High-precision real-time 3D shape measurement using a bi-frequency scheme and multi-view system

TIANYANG TAO,[1,2] QIAN CHEN,[2] SHIJIE FENG,[1,2] YAN HU,[1,2] JIAN DA,[1,2] AND CHAO ZUO[1,2,*] [iD]

[1]*Smart Computational Imaging (SCI) Laboratory, Nanjing University of Science and Technology, Nanjing, Jiangsu Province 210094, China*
[2]*Jiangsu Key Laboratory of Spectral Imaging & Intelligent Sense, Nanjing University of Science and Technology, Nanjing, Jiangsu Province 210094, China*
Corresponding author: surpasszuo@163.com

High-speed and high-precision 3D shape measurement plays a central role in diverse applications such as automatic online inspection, robotics control, and human-computer interaction. Conventional multi-frame phase-shifting-based fringe projection profilometry techniques face inherent trade-offs between the speed and measurement precision, which are fundamentally limited by the fringe density and extra pattern projections used for de-ambiguity of fringe orders. Increasing the frequency of the projection fringes can obviously improve the measurement precision; however, it creates difficulties in the subsequent phase unwrapping. For this reason, to date, the frequency of the fringes in typical real-time 3D shape measurement techniques is generally less than 30 to guarantee a reasonable reliability of phase unwrapping. To overcome this limitation, a bi-frequency phase-shifting technique based on a multi-view fringe projection system is proposed, which significantly enhances the measurement precision without compromising the measurement speed. Based on the geometric constraints in a multi-view system, the unwrapped phase of the low-frequency (10-period) fringes can be obtained directly, which serves as a reference to unwrap the high-frequency phase map with a total number of periods of up to 160. Besides, the proposed scheme with 10-period and 160-period fringes is suitable for slightly defocusing projection, allowing a higher projection rate and measurement speed. Experiments on both static and dynamic scenes are performed, verifying that our method can achieve high-speed and high-precision 3D measurement at 300 frames per second with a precision of about 50 μm. © 2017 Optical Society of America

OCIS codes: (120.0120) Instrumentation, measurement, and metrology; (150.6910) Three-dimensional sensing; (120.5050) Phase measurement; (150.0150) Machine vision.

https://doi.org/10.1364/AO.56.003646

1. INTRODUCTION

Optical three-dimensional (3D) measurement is playing a significant role in both scientific and industrial areas due to its non-contact nature [1]. Among these optical approaches, fringe projection profilometry (FPP) has proven to be one of the most promising techniques for high-resolution whole-field 3D reconstruction, especially for measuring the motion or deformation of dynamic objects [2–5] with the rapid development of the digital mirror device (DMD). Fourier transform profilometry (FTP) [6–11] and phase-shifting profilometry (PSP) [12–16] are the mainstream techniques in FPP, and in this field the primary task is to improve the measurement precision and decrease the sensitivity to dynamic scenes.

To reduce the potential motion artifacts, some researchers proposed FTP [6–11] by which only a single fringe pattern is sufficient to retrieve the phase. High efficiency in phase retrieval enables FTP to perform well in real-time 3D shape measurement, but the measured surface is supposed to be geometrically simple to avoid spectral overlapping problem. A valid method that can refrain from this frequency problem is π phase-shifting FTP [17] by adding another fringe pattern. However, the measurement accuracy is still seriously limited by information about the noise and bandwidth of the modulating signals of the pattern to be analyzed, and up to now, how to increase the measurement accuracy of FTP is still a challenge.

Compared to FTP, PSP has the advantages of higher accuracy, larger resolution, and greater insensitivity to ambient light [18–21]. This method has been extensively applied in static 3D measurement and can achieve high precision by simply projecting a large number of low- and high-density fringe patterns. The rapid development of the DMD technique in recent years endows PSP with the ability of dynamic 3D measurement by increasing projection speed of the fringe patterns, which is another way to reduce motion artifacts [12–16]. Being different from static measurement, dynamic measurement requires a

small number of projection patterns. The minimum number of projection patterns in the phase-shifting method is three, and the spatial phase unwrapping approach [22–24] is utilized to obtain the absolute phase. However, the spatial phase unwrapping algorithm fails in regions with depth discontinuities (complex surface) [25]. To measure complex surface, a temporal phase unwrapping algorithm [26–30] has to be used in which several additional fringe patterns are projected to obtain an auxiliary phase for phase unwrapping. Assuming the ambient light keeps constant in a short time, the total number of projection patterns can be decreased to five by using bi-frequency phase shifting scheme [16]. This approach has been successfully demonstrated for high-speed (kHz) [16] and real-time [31] 3D shape measurements of dynamic scenes. But in order to unwrap the phase accurately, the frequency of the high-density fringes is restricted to about 20 due to the limitation of the number of projection patterns. It is well known that under the same conditions, low density fringes generally result in a phase with low sensitivity, so the measurement precision is still much lower than the multi-frequency method (number of frequency ≥ 3) applied in static measurement. Besides the spatial phase unwrapping algorithm and the temporal phase unwrapping algorithm, a novel phase unwrapping scheme, the geometric constraints phase unwrapping algorithm, was introduced to FPP [32]. Several approaches based on this basic principle were proposed, and the real-time 3D profilometry using minimum fringe patterns comes true [33–36]. Some of these methods, such as [34] and [35], can realize high-precision measurement by using high-density fringes, but the measurement volume must be restricted to a small area.

Dozens of FPP approaches have been proposed, and they have made important contributions to this field. However, the trade-offs between the measurement speed and precision are unavoidable to guarantee the robustness of phase unwrapping. The real-time or high-speed FPP methods often focus on the measurement speed, and the number of projection patterns is severely restricted to decrease the motion error. In this case, adopting low-frequency fringes is in accordance with the priority of reliable phase unwrapping but obtains low measurement precision. The static schemes, on the contrary, stably retrieve absolute phase of high-frequency fringes by projecting quite a number of reference patterns so the measurement precision is much higher, but they are applicable only for static scenes. In this paper, we present a bi-frequency phase-shifting technique based on a multi-view system to increase the fringe density with five projection patterns so that the measurement precision can be improved greatly in real-time 3D shape measurement. Two low-frequency fringe patterns and three high-frequency fringe patterns are projected onto the measured objects, and the two related phase maps can be calculated from these fringes, respectively. Then the low-frequency phase map is unwrapped directly by the geometric constraint, and the obtained absolute phase map is utilized to calculate the high-frequency one through multi-frequency phase unwrapping, which has proven to be more accurate than other temporal phase unwrapping algorithms [26]. Besides, the proposed scheme with 10-period and 160-period fringes is suitable for slightly defocusing projection, allowing for higher projection rate and measurement speed.

2. PRINCIPLE

A. Three-Step Phase-Shifting Algorithm

The N-step phase-shifting algorithm is a well-known method in PSP due to its insensitivity to the surface reflectivity and ambient light. A set of phase-shifting sinusoidal patterns are projected, and the minimum number of images is three. Provided that both the ambient light and the reflectivity keep constant then within a short period, the three standard phase-shifting fringe patterns with shift offset of $2\pi/3$ are captured as

$$
\begin{aligned}
I_1 &= A + B_L \cos \phi_L, \\
I_2 &= A + B_L \cos(\phi_L + 2\pi/3), \\
I_3 &= A + B_L \cos(\phi_L + 4\pi/3),
\end{aligned}
\tag{1}
$$

where I_1, I_2, and I_3 are the recorded intensities, A is the DC component, B_L is the signal amplitude, and ϕ_L is the phase. The phase ϕ_L corresponds to projector coordinates and height coordinates derived as [37]

$$
Z = f(\phi_L), x_p = \frac{\phi_L W}{2\pi N_L},
\tag{2}
$$

where x_p is the projector x coordinate, W is the horizontal resolution of the projection pattern, N_L is the number of periods of the sinusoidal fringes, and Z is the height in 3D space. This means if phase ϕ_L is known, the 3D position can be calculated using calibration parameters between the camera and the projector [37]. The wrapped phase φ_L can be calculated as follows [12]:

$$
\varphi_L = \arctan \frac{\sqrt{3}(I_3 - I_2)}{2I_1 - I_2 - I_3}.
\tag{3}
$$

The relationship between ϕ_L and φ_L is

$$
\phi_L = \varphi_L + 2k\pi, \qquad k \in [0, N_L - 1],
\tag{4}
$$

where k is the period order. If the N_L is chosen as one then for all the points in the wrapped phase, we have $\phi_L = \varphi_L$, which means the height information of each point is available. Larger N_L will improve the phase precision, but in this case, confirming the k of an arbitrary point needs a further algorithm. Temporal phase unwrapping is the robust algorithm to eliminate period ambiguities by the projection of multi-group fringe patterns with different frequencies [26]. To decrease the motion artifacts, the number of fringe patterns should be as small as possible, so the bi-frequency scheme becomes the most commonly used method in dynamic measurement. Generally, at least six fringe patterns are necessary to conduct temporal phase unwrapping. In a high-speed projection system, the ambient light can be considered a constant value in a short period, so the minimum number of the fringe patterns in the bi-frequency scheme can be reduced to five. This property is utilized in [16] by projecting other two patterns with different fringe frequencies

$$
\begin{aligned}
I_4 &= A + B_H \sin \phi_H \\
I_5 &= A + B_H \cos \phi_H,
\end{aligned}
\tag{5}
$$

to get another phase map φ_H, where I_4, I_5 are the recoded intensities, B_H is the signal amplitude, and ϕ_H is the absolute phase. As the average intensity A is a constant value in $I_1 - I_5$, we can easily derive

$$A = \frac{I_1 + I_2 + I_3}{3} \qquad (6)$$

from Eq. (1). Then the wrapped phase is formulated as

$$\varphi_H = \frac{I_4 - A}{I_5 - A}. \qquad (7)$$

Finally, the two phases with different frequencies (φ_H and φ_H) can be unwrapped with each other by temporal phase unwrapping approaches.

However, to guarantee the reliability of phase unwrapping, the frequencies of the fringes are still less than 30. Three mainstream temporal phase unwrapping methods have been proposed [26], and the multi-frequency approach performs most reliably among the three kinds of algorithms. But the one-period fringes serving as auxiliary fringes also restrict the frequency of high-density fringes. Increasing the frequency of the auxiliary fringes becomes the direct method to reliably obtain absolute phase of higher-density fringes in the bi-frequency scheme. The key to this problem is how to directly unwrap the phase of the auxiliary fringes when these fringes are not one period.

B. Phase Unwrapping for 10-Period Fringes

Geometric constraints in a multi-view system are widely applied in the image correlation area because it can increase the efficiency of exploring the corresponding point. Generally speaking, an arbitrary point p in one perspective corresponds to a straight line in 3D space, and the projection segment of this line in another perspective. Supposing that the images to be correlated are wrapped phase maps, according to Eq. (2) p has N_L corresponding points (also called candidates in this paper) in 3D space, and this is shown in Fig. 1. It is a fact that the measurement volume in our system is not infinite, and the estimated depth range is known in advance so the corresponding points beyond this depth range can be rejected. As shown in Fig. 1, only a few numbers of points between $Z_{\min}$ and $Z_{\max}$ remain to be confirmed in the further process. The number of these retained points is restricted by the depth range [$Z_{\min}$, $Z_{\max}$] as well as the fringe density N_L. In order to explain the relationships qualitatively, Eq. (2) is rewritten as [15]

$$Z = M_Z + \frac{N_Z}{C_Z x_p + 1}, x_p = \frac{\phi_L W}{2\pi N_L}, \qquad (8)$$

where M_Z, N_Z, and C_Z are the constants derived from calibration parameters. Once the system (or calibration parameters)
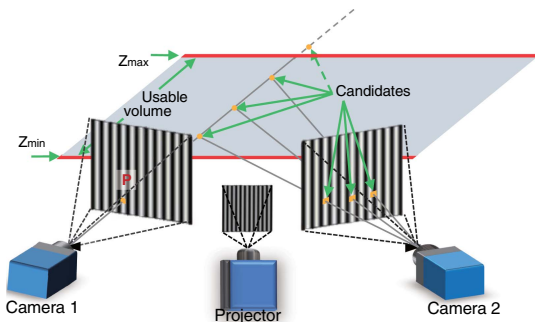

Fig. 1.   Illustration of an arbitrary point p in one camera and its corresponding points in 3D space and another camera.

and the measurement depth range are fixed, the smaller N_L is, the longer the spacing between the adjacent candidates is, which implies the less candidates will remain. In this system, the values of $Z_{\min}$ and $Z_{\max}$ are set to –200 mm and 200 mm, respectively. Besides, N_L is equal to 10, then about one or two candidates are reserved and projected to another wrapped phase map from the second camera. The projection point having the nearest phase value with p is eventually selected as the correct corresponding point. Now, we could obtain an unwrapped phase map of 10-period fringes as well as the "coarse" 3D reconstruction result with a relative low precision.

C. Precision Analysis and Improvement

Through the three-step phase-shifting algorithm and geometric constraints, an absolute phase map of 10-period fringes is obtained, but the final measurement precision calculated with this map still needs improvement. The essential factor affecting precision is the noise, and the captured images I_i^n in Eq. (1) should be rewritten as

$$I_i^n = I_i + n_i. \qquad (9)$$

To simplify our analysis, we assume that the noise is additive Gaussian random variable $n_i \sim N(0, \sigma_n)$. Then the wrapped phase φ_L^n can be calculated by substituting Eq. (9) into Eq. (3):

$$\varphi_L^n = \frac{\sqrt{3}(I_3 - I_2) + N_1}{2I_1 - I_2 - I_3 + N_2}, \qquad (10)$$

where $N_1 = \sqrt{3}(n_3 - n_2)$, $N_2 = 2n_1 - (n_2 + n_3)$. Auxiliary variables N_1 and N_2 also obey the Gaussian distribution, i.e., $N_1 \sim N(0, 6\sigma_n^2)$ and $N_2 \sim N(0, 6\sigma_n^2)$. The measured phase can be considered as the sum of the actual phase and the phase error caused by the noise. Thus, we have

$$\Delta\varphi_L = \varphi_L^n - \varphi_L = \frac{N_1 \cos \phi_L - N_2 \sin \phi_L}{3B_L + N_2 \cos \phi_L + N_1 \sin \phi_L}. \qquad (11)$$

Usually, the noise is usually much smaller than the intensity modulation $3B_L$, so Eq. (11) can be further approximated as

$$\Delta\varphi_L = \frac{N_1 \cos \phi_L - N_2 \sin \phi_L}{3B_L}. \qquad (12)$$

According to the analysis in [18,26], the variance of the phase error $\sigma_{\Delta\varphi_L}$ can be represented as

$$\sigma_{\Delta\varphi_L}^2 \approx \frac{6\sigma_n^2(\cos \phi_L^2 + \sin \phi_L^2)}{(3B_L)^2} = \left(\frac{\sqrt{6}\sigma_n}{3B_L}\right)^2. \qquad (13)$$

It is implied in Eq. (13) that $\sigma_{\Delta\varphi_L}$ linearly increases with σ_n, and decreases with B_L. It should be noted that the absolute phase has the same phase error as $\sigma_{\Delta\varphi_L}$ from Eq. (13), and this phase error is marked as $\sigma_{\Delta\phi_L}$. However, the $\sigma_{\Delta\phi_L}$ should be scaled into the dynamic range $[0, 2\pi)$ when converted to the 3D coordinate in Eq. (2), which means the equivalent phase error of $\sigma_{\Delta\phi_L}$ decreases with N_L. Because σ_n and B_L are difficult to optimize, increasing the value of N_L becomes the most effective method to improve the precision of ϕ_L. Certainly, it is difficult to increase the N_L directly according to the analysis in Section 2.B, and an advisable method is to project extra fringe patterns with higher frequency. Supposing the ambient light in a short time keeps constant, then by adding two high-frequency fringe patterns,

$$I_4^n = A + B_H \sin \phi_H + n_4, \quad I_5^n = A + B_H \cos \phi_H + n_5, \tag{14}$$

we are able to achieve the high-density wrapped phase φ_H^n with the fringe periods N_H ($N_H \gg N_L$):

$$\varphi_H^n = \arctan \frac{I_4^n - A^n - n_4}{I_5^n - A^n - n_5}, \tag{15}$$

where $A^n = (n_1 + n_2 + n_3)/3$. The phase error $\sigma_{\Delta\varphi_H}$ of φ_H^n, referring to Eqs. (9)–(13), is

$$\sigma_{\Delta\varphi_H}^2 \approx \frac{12\sigma_n^2(\cos \phi_H^2 + \sin \phi_H^2)}{(3B_H)^2} = \left(\frac{\sqrt{12}\sigma_n}{3B_H}\right)^2. \tag{16}$$

It is the same as $\sigma_{\Delta\phi_H}$ of ϕ_H^n, where ϕ_H^n is the calculated unwrapped phase, and the equivalent phase error is $\sqrt{12}\sigma_n/3B_H N_H$, where $\sqrt{12}\sigma_n/3B_H N_H \ll \sqrt{6}\sigma_n/3B_L N_L$. This bi-frequency scheme can be called the "2H + 3L" scheme, and there exists another alternative scheme called the "3H + 2L" scheme to obtain a high-frequency wrapped phase map with the same scheme but exchanging the periods of two sets of fringe patterns.

The captured images in the 3H + 2L scheme are shown as

$$J_1^n = A + B_H \cos \Psi_H + n_1,$$
$$J_2^n = A + B_H \cos(\Psi_H + 2\pi/3) + n_2,$$
$$J_3^n = A + B_H \cos(\Psi_H + 4\pi/3) + n_3,$$
$$J_4^n = A + B_L \sin \Psi_L + n_4,$$
$$J_5^n = A + B_L \cos \Psi_L + n_5. \tag{17}$$

Here, we make a reasonable assumption that the average intensity A and the modulations B_H and B_L in this 3H + 2L scheme are the same as those in the 2H + 3L scheme. Ψ_H and Ψ_L are the unwrapped phases of high-frequency fringes and low-frequency fringes in the 3H + 2L scheme, respectively. According to the previous analysis, the phase errors of the wrapped phases ψ_H^n and ψ_L^n in this scheme are

$$\sigma_{\Delta\psi_H}^2 \approx \frac{6\sigma_n^2(\cos \Psi_H^2 + \sin \Psi_H^2)}{(3B_H)^2} = \left(\frac{\sqrt{6}\sigma_n}{3B_H}\right)^2,$$
$$\sigma_{\Delta\psi_L}^2 \approx \left(\frac{\sqrt{12}\sigma_n}{3B_L}\right)^2, \tag{18}$$

and the equivalent error $\sigma_{\Delta\Psi_H}$ of Ψ_H^n is $\sqrt{6}\sigma_n/3B_H M_H$, where M_H is the number of periods of high-frequency fringes in 3H + 2L scheme.

To further analyze the minimum equivalent error of these two schemes, we should evaluate upper limits to the values of N_H, M_H, and B_H. The first limitation of the maximum value of N_H or M_H is the noise. To explain the relationship between the noise and N_H, Eq. (4) is updated as

$$\phi_H^n = \varphi_H^n + 2k_H\pi, \quad k_H = \text{Round}\left(\frac{N_H\phi_L^n - \varphi_H^n}{2\pi}\right), \tag{19}$$

where "Round" represents the rounding function. To round the value of $(N_H\phi_L^n - \varphi_H^n)/2\pi$ to the correct integer, we should guarantee [26]

$$\left|\frac{N_H\phi_L^n - \varphi_H^n}{2\pi} - \frac{N_H\phi_L - \varphi_H}{2\pi}\right| < 0.5. \tag{20}$$

In the 2H + 3L scheme, Eq. (20) can be replaced with

$$\frac{\sqrt{6}\sigma_n N_H}{3B_L N_L} + \frac{\sqrt{12}\sigma_n}{3B_H} < \pi, \tag{21}$$

because the maximum value of noise is unknown; here, the standard deviation σ_n is utilized to conduct a simple analysis. Eq. (21) can be further simplified as

$$N_H < \frac{C - \sqrt{12}}{\sqrt{6}} N_L, \tag{22}$$

where $C = 3B_H\pi/\sigma_n$ (assuming $B_H = B_L$). Finally, the equivalent phase error $\sigma_{\Delta\phi_H}$ meets the following inequality:

$$\sigma_{\Delta\phi_H} > \frac{2\sqrt{2}\sigma_n}{(C - \sqrt{12})B_H N_L}. \tag{23}$$

In the 3H + 2L scheme, some similar inequalities,

$$M_H < \frac{C - \sqrt{6}}{\sqrt{12}} M_L, \quad \sigma_{\Delta\Psi_H} > \frac{2\sqrt{2}\sigma_n}{(C - \sqrt{6})B_H M_L}, \tag{24}$$

are obtained, where M_L is the number of periods of low-frequency fringes in the 3H + 2L scheme, and it is same as N_L. We can find the precision in these two schemes is almost the same based on the fact that $\sqrt{12} \ll C$. To verify this conclusion, simulations are provided here with $B_H = 0.5$, $\sigma_n = 0.05$, $N_L = 1$, and $M_L = 1$, and the results are shown in Fig. 2. The error rate in this figure is the difference ratio between the absolute phase of the fringes with and without noise. Note that the errors at the edge of the phase map are ignored, which has been found to be a common issue in current temporal phase unwrapping approaches [26]. The 2H + 3L scheme has a smaller error rate than the 3H + 2L scheme; in other words, the 2H + 3L scheme can unwrap higher frequency fringes under the same error. From Figs. 2(b), 2(c), 2(e), and 2(f), we can find the number of fringe periods with the same error rate in the 2H + 3L scheme is $\sqrt{2}$ times than the other one, which verifies the conclusions in Eqs. (23) and (24). However, the precision of the 3H + 2L scheme is $\sqrt{2}$ times higher if N_H is equal to M_H. If we consider just the effect of noise, these two methods should have the same precision, but other limitations, such as the resolution of the projector, will also have an impact on the final measurement precision.
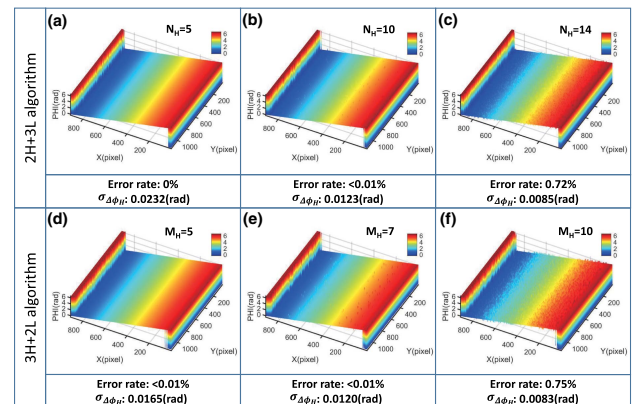

Fig. 2. Simulation results of the 2H + 3L scheme and 3H + 2L scheme under different N_H and M_H.

In other words, the 3H + 2L scheme can achieve the same measurement precision as the 3L + 2H scheme in the presence of noise based on the phase measurement with 3 high-frequency fringe patterns with less periods. This property makes the 3H + 2L scheme more robust to the defocusing blur. Besides, the finite sampling effect of the projector pixel also imposes a limit on the highest possible fringe density of high-frequency patterns. Both the resolution restriction and the defocus effect make the 3H + 2L scheme superior to the 2H + 3L scheme, and for these reasons the 3H + 2L scheme is adopted in our experiments.

3. EXPERIMENTS

A high-speed FPP system is set up to validate the properties of the proposed method. This system includes a digital light processing (DLP) projector (Light Crafter 4500) with resolution of 912×1140 and two digital CMOS cameras (AVT GigE Mako G-030B) with a maximum frame rate of 309 frames per second (fps) under the 644×484 resolution. The cameras are synchronized with the projector using the pulse signal sent out by DLP.

First, a ceramic plate was measured by the traditional method and the proposed method. The specific improvement of precision in the phase and the 3D coordinate is presented by the comparison results of this static experiment. Second, we tested a moving palm to verify the feasibility of 3D measurement in dynamic scenes with high precision. Last, the 8-bit fringe patterns are replaced with the 6-bit fringe patterns to realize the high-speed FPP at 300 fps in slightly defocused condition.

A. Precision Analysis

A ceramic plate was measured to verify the improvement in precision. This ceramic plate has the precision of 1 µm so it is qualified to serve as a standard planar surface. To ensure the success rate in phase unwrapping, two one-period fringe patterns and three 24-period fringe patterns are applied in the conventional bi-frequency phase shifting method. In the proposed method, the number of fringe periods with the low frequency is 10, and the higher one is 160. 160-period fringes are utilized to validate that the proposed algorithm can obtain an absolute phase of high-density fringes easily and simultaneously guarantee good modulation of the captured fringes. This experiment includes testing the precision improvement of the unwrapped phase and the final 3D reconstruction. Figure 3 plots the local detail, where Figs. 3(c) and 3(d) represent the phase error of line 333 in the unwrapped phase of 24-period fringes and 160-period fringes, respectively. The standard deviation in Fig. 3(c) is 3.41 times of that in Fig. 3(d), which seems to not match our theortical prediction in Section 3.3. However, when the density of the fringes is relatively large, the attenuation of the modulation B_H due to defocus should not be neglected, and note that the average value of modulation in Fig. 3(b) is 0.53, nearly half the value in Fig. 3(a). So the theoretical improvement of the precision for the phase is $160 \times 0.53/24 = 3.56$, and it agrees well with the experiment result. According to Eq. (8), we can estimate the improvement of 3D reconstruction, and the result is
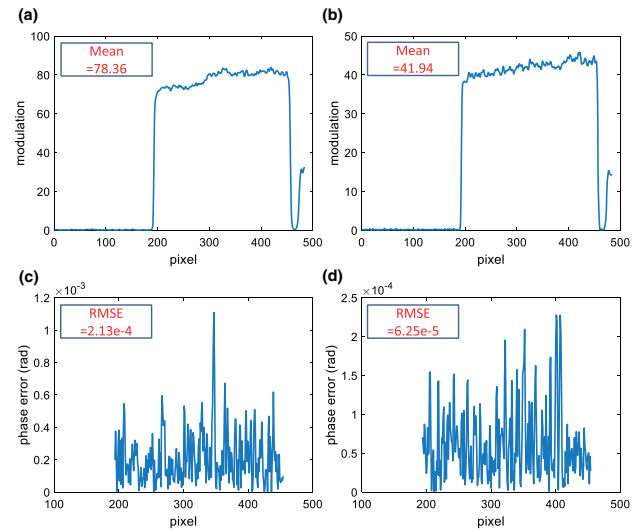

Fig. 3. Detailed results of line 333 in the unwrapped phase map and the modulation map. (a) Results of line 333 in the modulation map of 24-period fringes. (b) Results of line 333 in the modulation map of 160-period fringes. (c) Results of line 333 in the unwrapped phase map of 24-period fringes. (d) Results of line 333 in the unwrapped phase map of 160-period fringes.

$$\frac{x_{\Delta\Psi_{24}}}{x_{\Delta\Psi_{160}}} \left[\frac{C_Z(x_p + x_{\Delta\Psi_{160}}) + 1}{C_Z(x_p + x_{\Delta\Psi_{24}}) + 1} \right] \approx \frac{x_{\Delta\Psi_{24}}}{x_{\Delta\Psi_{160}}} = 3.41, \text{ where } x_{\Delta\Psi_{160}} = \frac{\Delta\Psi_{160}W}{2\pi \cdot 160},$$

$x_{\Delta\Psi_{24}} = \frac{\Delta\Psi_{24}W}{2\pi \cdot 24}, \Delta\Psi_{160} = \Psi_{160}^n - \Psi_{160}, \text{ and } \Delta\Psi_{24} = \Psi_{24}^n - \Psi_{24}.$ The 3D reconstruction result of the ceramic plate is shown in Fig. 4, Figures 4(d) and 4(e) stand for the height of line 333 in Figs. 4(a) and 4(b). This result implies that the precision of the proposed method is 46.2 µm, about 3.42 times the traditional scheme. Because of the application of high-density fringes, our system is suitable for the defocusing technique so that the 160-period 6-bit fringes can be translated into sinusoidal fringes easily under slightly defocused condition. Figures 4(c) and 4(f) are the related results using 6-bit patterns; the precision 53.7 µm is still much higher than the traditional method.

B. Real-Time and High-Speed Measurement

Next, we tested a moving palm to illustrate the performance of our system for measuring dynamic scenes. To emphasize the
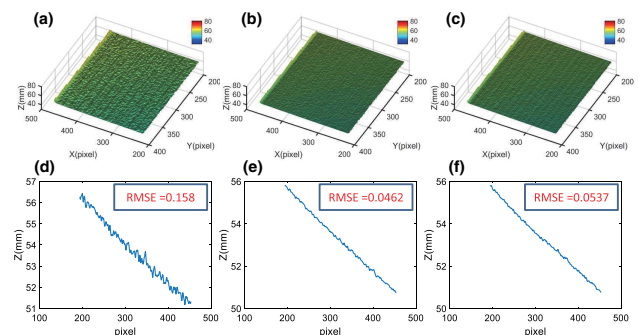

Fig. 4. 3D reconstruction results of the ceramic plate. (a) Global 3D reconstruction result of the traditional method. (b) Global 3D reconstruction result of the proposed method. (c) Global 3D reconstruction result of the proposed method using 6-bit fringes. (d)–(f) Results of line 333 in (a)–(c).
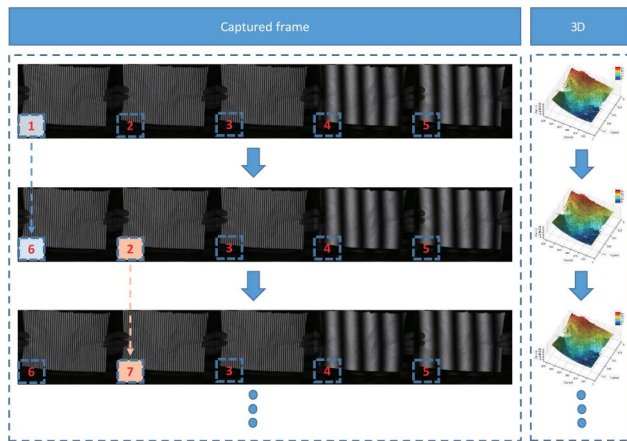
Fig. 5. Framework of real-time 3D reconstruction.

details in 3D reconstruction, the images captured synchronously were processed in MATLAB under the appropriate rendering. Note that once a new frame is captured, a new 3D reconstruction is performed based on a sliding-window reconstruction scheme, as shown in Fig. 5. This operation is reasonable because the speed of projection in our system is fast enough.
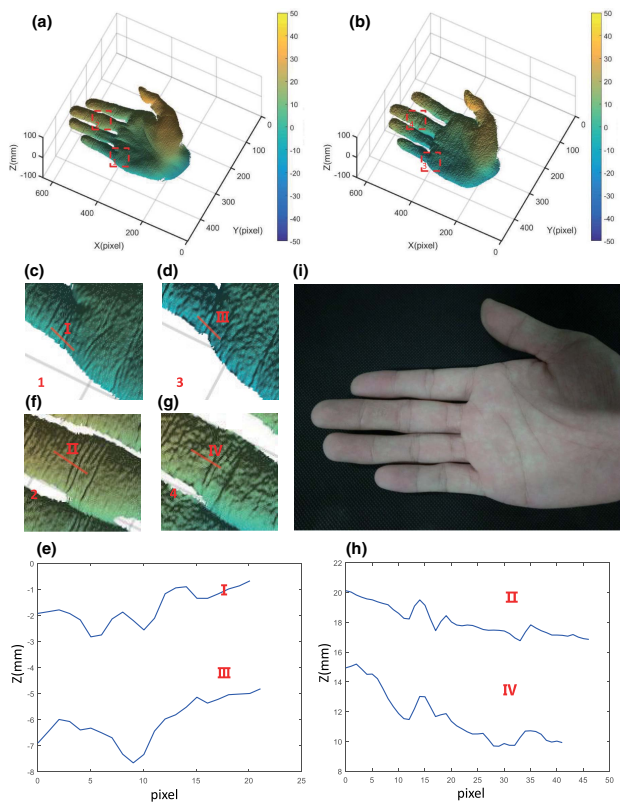

Fig. 6. 3D reconstruction results of the moving palm (see associated Visualization 1). (a) 3D reconstruction result of the proposed method. (b) 3D reconstruction result of the traditional method. (c) Enlargement of the local area in (a). (d) Enlargement of the local area in (b). (e) Height curves of the segments in (c) and (d). (f) Enlargement of the local area in (a). (g) Enlargement of the local area in (b). (h) Height curves of the segments in (f) and (g). (i) Measured palm.
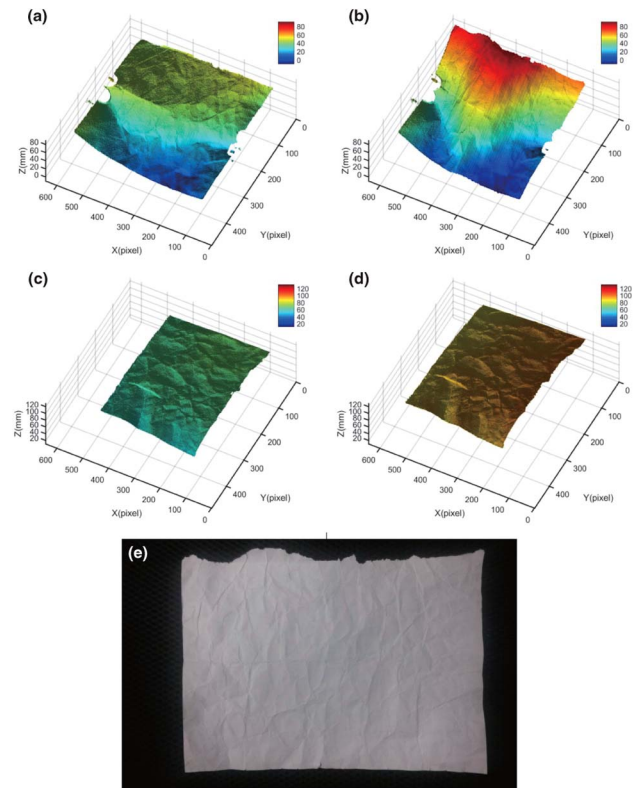

Fig. 7. 3D reconstruction results of a wrinkled paper (see also associated Visualization 2 and Visualization 3). (a) and (b) Samples of 3D reconstruction results of (e) in deformation process. (c) and (d) Samples of 3D reconstruction results of (e) in dithered condition. (e) Wrinkled paper.

The palm is a discontinuous surface so it can also be utilized to validate the robustness of the proposed method. Figure 6 displays the 3D reconstruction results, and more comparative results are shown in Visualization 1. From Figs. 6(c)–6(h), we can see that the tiny details of the palm in the proposed method remain but are lost in the traditional method.

The fringes in our scheme are 10-period and 160-period, where the 160-period fringes can keep sinusoidal property in nearly focused condition, even if a lower bit fringe pattern is used. Though the 10-period lower bit fringes cannot reach the same sinusoidality, the calculated phase from these fringes is only used for unwrapping of the high-frequency phase, and thus, will have no impact on the final reconstruction result. Then we substituted 6-bit fringes for these 8-bit fringes to further increase the projection rate and measurement speed. The related measurement results are shown in Fig. 7 (see also associated Visualization 2 and Visualization 3). The speed of projection is able to reach 480 fps, but, restricted by the captured speed of 309 fps of the camera, these experiments were implemented in 300 fps.

4. CONCLUSION

In conclusion, we have proposed a bi-frequency scheme to improve the measurement precision for real-time 3D shape

measurement. Benefitting from the geometric constraint in a multi-view system, an absolute phase map of 10-period fringes can be calculated directly, and then this map serves as a reference to unwrap the phase of 160-period fringes. These high-density fringes greatly improve measurement precision, which is often neglected by conventional real-time approaches. Compared to existing approaches, only five fringe patterns are required for one high-quality reconstruction, making this scheme highly suitable for high-speed high-precision 3D shape measurement of dynamic scenes. Besides, the proposed scheme with 10-period and 160-period fringes is suitable for slightly defocusing projection, allowing a higher projection rate and measurement speed. Experiments verified its validity and effectiveness for high-precision and real-time 3D shape measurement. Finally, it should be mentioned that when 4-bit fringes are used, the ripple emerges so that only 6-bit fringes are applied in this paper. Fringe optimization based on more complicated dithering algorithm is expected to provide further improvement on both the projection speed and the measurement precision, which is an interesting direction for future work.

REFERENCES

1. F. Chen, G. M. Brown, and M. Song, "Overview of three-dimensional shape measurement using optical methods," Opt. Eng. **39**, 10–22 (2000).
2. S. S. Gorthi and P. Rastogi, "Fringe projection techniques: whither we are?" Opt. Lasers Eng. **48**, 133–140 (2010).
3. X. Su and Q. Zhang, "Dynamic 3-d shape measurement method: a review," Opt. Lasers Eng. **48**, 191–204 (2010).
4. S. Zhang, "Recent progresses on real-time 3d shape measurement using digital fringe projection techniques," Opt. Lasers Eng. **48**, 149–158 (2010).
5. S. Van der Jeught and J. J. Dirckx, "Real-time structured light profilometry: a review," Opt. Lasers Eng. **87**, 18–31 (2016).
6. M. Takeda and K. Mutoh, "Fourier transform profilometry for the automatic measurement of 3-d object shapes," Appl. Opt. **22**, 3977–3982 (1983).
7. Q. Zhang and X. Su, "High-speed optical measurement for the drumhead vibration," Opt. Express **13**, 3110–3116 (2005).
8. X. Su and W. Chen, "Fourier transform profilometry: a review," Opt. Lasers Eng. **35**, 263–284 (2001).
9. S. Feng, Q. Chen, and C. Zuo, "Graphics processing unit-assisted real-time three-dimensional measurement using speckle-embedded fringe," Appl. Opt. **54**, 6865–6873 (2015).
10. Q. Kemao, "Two-dimensional windowed Fourier transform for fringe pattern analysis: principles, applications and implementations," Opt. Lasers Eng. **45**, 304–317 (2007).
11. L. Huang, Q. Kemao, B. Pan, and A. K. Asundi, "Comparison of fourier transform, windowed fourier transform, and wavelet transform methods for phase extraction from a single fringe pattern in fringe projection profilometry," Opt. Lasers Eng. **48**, 141–148 (2010).
12. V. Srinivasan, H.-C. Liu, and M. Halioua, "Automated phase-measuring profilometry of 3-d diffuse objects," Appl. Opt. **23**, 3105–3108 (1984).
13. C. Zuo, Q. Chen, G. Gu, S. Feng, and F. Feng, "High-speed three-dimensional profilometry for multiple objects with complex shapes," Opt. Express **20**, 19493–19510 (2012).
14. Y. Gong and S. Zhang, "Ultrafast 3-d shape measurement with an off-the-shelf dlp projector," Opt. Express **18**, 19743–19754 (2010).
15. K. Liu, Y. Wang, D. L. Lau, Q. Hao, and L. G. Hassebrook, "Dual-frequency pattern scheme for high-speed 3-d shape measurement," Opt. Express **18**, 5229–5244 (2010).
16. C. Zuo, Q. Chen, G. Gu, S. Feng, F. Feng, R. Li, and G. Shen, "High-speed three-dimensional shape measurement for dynamic scenes using bi-frequency tripolar pulse-width-modulation fringe projection," Opt. Lasers Eng. **51**, 953–960 (2013).
17. L. Guo, X. Su, and J. Li, "Improved fourier transform profilometry for the automatic measurement of 3d object shapes," Opt. Eng. **29**, 1439–1444 (1990).
18. J. Li, L. G. Hassebrook, and C. Guan, "Optimized two-frequency phase-measuring-profilometry light-sensor temporal-noise sensitivity," J. Opt. Soc. Am. A **20**, 106–115 (2003).
19. X.-Y. Su, G. Von Bally, and D. Vukicevic, "Phase-stepping grating profilometry: utilization of intensity modulation analysis in complex objects evaluation," Opt. Commun. **98**, 141–150 (1993).
20. S. Feng, Y. Zhang, Q. Chen, C. Zuo, R. Li, and G. Shen, "General solution for high dynamic range three-dimensional shape measurement using the fringe projection technique," Opt. Lasers Eng. **59**, 56–71 (2014).
21. Y. Hu, Q. Chen, T. Tao, H. Li, and C. Zuo, "Absolute three-dimensional micro surface profile measurement based on a greenough-type stereomicroscope," Meas. Sci. Technol. **28**, 045004 (2017).
22. S. Zhang, X. Li, and S.-T. Yau, "Multilevel quality-guided phase unwrapping algorithm for real-time three-dimensional shape reconstruction," Appl. Opt. **46**, 50–57 (2007).
23. S. Yuqing, "Robust phase unwrapping by spinning iteration," Opt. Express **15**, 8059–8064 (2007).
24. M. Costantini, "A novel phase unwrapping method based on network programming," IEEE Trans. Geosci. Remote Sens. **36**, 813–821 (1998).
25. J. M. Huntley and H. O. Saldner, "Error-reduction methods for shape measurement by temporal phase unwrapping," J. Opt. Soc. Am. A **14**, 3188–3196 (1997).
26. C. Zuo, L. Huang, M. Zhang, Q. Chen, and A. Asundi, "Temporal phase unwrapping algorithms for fringe projection profilometry: a comparative review," Opt. Lasers Eng. **85**, 84–103 (2016).
27. D. S. Mehta, S. K. Dubey, M. M. Hossain, and C. Shakher, "Simple multifrequency and phase-shifting fringe-projection system based on two-wavelength lateral shearing interferometry for three-dimensional profilometry," Appl. Opt. **44**, 7515–7521 (2005).
28. G. Pedrini, I. Alexeenko, W. Osten, and H. J. Tiziani, "Temporal phase unwrapping of digital hologram sequences," Appl. Opt. **42**, 5846–5854 (2003).
29. J. Zhu, P. Zhou, X. Su, and Z. You, "Accurate and fast 3d surface measurement with temporal-spatial binary encoding structured illumination," Opt. Express **24**, 28549–28560 (2016).
30. P. Zhou, J. Zhu, X. Su, Z. You, H. Jing, C. Xiao, and M. Zhong, "Experimental study of temporal-spatial binary pattern projection for 3d shape acquisition," Appl. Opt. **56**, 2995–3003 (2017).
31. S. Feng, Q. Chen, C. Zuo, J. Sun, and S. L. Yu, "High-speed real-time 3-d coordinates measurement based on fringe projection profilometry considering camera lens distortion," Opt. Commun. **329**, 44–56 (2014).
32. T. Weise, B. Leibe, and L. Van Gool, "Fast 3d scanning with automatic motion compensation," in *2007 IEEE Conference on Computer Vision and Pattern Recognition* (IEEE, 2007), pp. 1–8.

33. D. Li, H. Zhao, and H. Jiang, "Fast phase-based stereo matching method for 3d shape measurement," in *Optomechatronic Technologies (ISOT), 2010 International Symposium on* (IEEE, 2010), pp. 1–5.

34. Z. Li, K. Zhong, Y. F. Li, X. Zhou, and Y. Shi, "Multiview phase shifting: a full-resolution and high-speed 3d measurement framework for arbitrary shape dynamic objects," Opt. Lett. **38**, 1389–1391 (2013).

35. C. Bräuer-Burchardt, A. Breitbarth, P. Kühmstedt, and G. Notni, "High-speed three-dimensional measurements with a fringe projection-based optical sensor," Opt. Eng. **53**, 112213 (2014).

36. T. Tao, Q. Chen, J. Da, S. Feng, Y. Hu, and C. Zuo, "Real-time 3-d shape measurement with composite phase-shifting fringes and multi-view system," Opt. Express **24**, 20253–20269 (2016).

37. S. Zhang and P. S. Huang, "Novel method for structured light system calibration," Opt. Eng. **45**, 083601 (2006).